Archives of Acoustics Vol. 51, No. 3, pp. 443–458 (2026), https://doi.org/10.24423/archacoust.2026.4353

Research Paper

Modeling and Investigation of a Multi-Resonant Metamaterial Sound Insulator

Zacharie Laly[(1)]*, Raymond Panneton[(1)], Noureddine Atalla[(1)], Sebastian Ghinet[(2)]

[(1)] *Centre for Research in Acoustics-Signal-Human of the Université de Sherbrooke*
Sherbrooke, Canada

[(2)] *National Research Council Canada, Aerospace*
Ottawa, Canada

*Corresponding Author: Zacharie.Laly@usherbrooke.ca

Received October 8, 2025; revised April 11, 2026; accepted April 15, 2026;
available online April 24, 2026; version of record July 16, 2026; published issue September 23, 2026.

A design of a multi-resonant acoustic metamaterial sound insulator is proposed to attenuate multi-tonal and broadband noise. The unit cell of the metamaterial consists of a porous material with four, nine, and sixteen embedded Helmholtz resonators and its sound attenuation performance is studied using the finite element method (FEM). A theoretical approach based on the transfer matrix method is proposed and the theoretical results of the sound absorption and the transmission loss (TL) agree well with FEM results. Compared to the porous layer with one embedded resonator that presents one TL and one sound absorption resonant peak, the metamaterial made of four, nine, and sixteen embedded resonators exhibits, respectively, four, nine, and sixteen sound absorption and TL resonant peaks. The sound absorption at various incidence angles and the diffuse field sound absorption of the proposed metamaterial are studied. At each resonant frequency, the acoustic pressure reaches its maximum in the cavity of the corresponding resonator while in the associated neck, the acoustic velocity peaks alongside significant acoustic power dissipation density. As the incidence angle increases, the acoustic pressure in the cavity at the resonant frequencies decreases as well as the velocity in the necks and the power dissipation density becomes negligible, resulting in a decrease of the sound absorption. As the number of resonators within the porous layer increases, the sound absorption and the TL frequency band enlarge. Compared to the conventional porous layer, the sound absorption, and the TL are significantly improved at the resonant frequencies of the resonators.

Keywords: porous material, Helmholtz resonators, sound absorption, transmission loss, acoustic metamaterial.



Copyright © 2026 The Author(s).
This work is licensed under the Creative Commons Attribution 4.0 International CC BY 4.0
(https://creativecommons.org/licenses/by/4.0/).

1. Introduction

Porous materials are widely used for noise reduction in many applications such as construction, transport, and manufacturing. Their microstructure featuring high porosity, a complex and interconnected pore network, and a large internal surface area allows the sound waves to enter the medium that dissipates their energy through viscous and thermal losses (Allard, Atalla, 2009). Porous materials are inefficient at low frequencies while they provide efficient sound dissipation at high frequencies. This limitation can be overcome by the use of inner inclusions within the porous layer. Boutin and Becot (2015) reported theoretical and experimental analysis on the acoustics of gas saturated rigid porous media with inner resonators. They observed that the resonators modify the effective bulk modulus of the medium which induces strong velocity dispersion and high attenuation around the resonance frequencies. They tested experimentally several prototypes of such media and compared the measurement with the theory. The sound attenuation performance of a cellular porous material with resonant inclusions was investigated by Doutres *et al.* (2015). Using theoretical, numerical and experimental approaches,

they demonstrated the transmission loss (TL) improvement of the material at the resonance frequency of the embedded Helmholtz resonator (HR). They illustrate that the impact of the resonator on the material's sound absorption performance can be positive or negative. Lagarrigue *et al.* (2013) studied the sound attenuation performance of porous material with arranged resonant inclusions (slotted cylinders) that are periodically embedded into the porous matrix and they observed the sound absorption improvement. Zhu *et al.* (2019) proposed a sound absorber composed of a porous layer embedded with periodic resonators made of two 180° twisted split rings. They demonstrated that a single resonator embedded in the porous material can achieve perfect absorption at its resonance frequency, which can be tuned by adjusting the resonator's inner radius. When four twisted split rings were incorporated into the porous layer, the sound absorption coefficient was improved. Abbad *et al.* (2019) studied a front membrane-cavity Helmholtz resonator embedded within a porous material and showed the transmission loss enhancement at the Helmholtz resonance. However, they found that the presence of the resonator can reduce the overall sound absorption performance, depending on the membrane's resonance frequency and they recommended the transmission configuration for application of the proposed design. Ghinet *et al.* (2020) studied the single and double wall configurations of glass wool layers with embedded periodic Helmholtz resonators for aircraft cabin applications. The TL of the studied design was experimentally evaluated under diffuse field excitation. Kone *et al.* (2021; 2022) investigated glass wool with an embedded resonator having a complex neck shape for aircraft cabin applications and they illustrated multiple sound absorption peaks. Magliacano *et al.* (2024) used the finite element method (FEM) and the transfer matrix method (TMM) to investigate the sound attenuation characteristics of porous material with an embedded periodic pattern such as hollow cylindrical inclusions, half-cut hollow cylindrical inclusions and Helmholtz resonators. The FEM results were compared with experiments. Helmholtz resonators with porous material lining were modeled by Zhang and Xin (2024) using the double porosity method. They demonstrated that the porous lining, as an additional damping helps to satisfy the impedance matching condition leading to the sound absorption improvement compared to the classic HR. Laly *et al.* (2022; 2023; 2024a) proposed transfer matrix methods to model acoustic metamaterial consisting of porous materials with embedded periodic Helmholtz resonators. The results of the TMM were validated by comparison with the FEM in single and double wall configurations. They demonstrated the impacts of the parameters of the periodic resonator on the TL and studied the influences of the elasticity of the resonator's walls on the sound attenuation performance (Laly *et al.*, 2024b). A porous material with a conventional embedded Helmholtz resonator provides only one resonant peak with a narrow frequency band.

In this study, a multi-resonant acoustic metamaterial based on a porous material with multiple embedded Helmholtz resonators is presented for multi-tonal and broadband noise reduction. The theoretical model using the transfer matrix method shows good agreement with the finite element method. The transmission loss and the diffuse field sound absorption of the metamaterial are significantly improved at the resonant frequencies of the resonators with the frequency band that increases as the number of resonators within the unit cell increases. The sound attenuation mechanism of the metamaterial is studied. The paper is organized as follows. In Sec. 2, the design of the proposed metamaterial is presented and Sec. 3 shows the theoretical modelling. The comparison of the theory with the finite element method is shown in Sec. 4 and the analysis of the sound attenuation performance is performed in Sec. 5 and finally the conclusion is presented in Sec. 6.

2. Finite element modeling of multi-resonant acoustic metamaterial

Low-frequency noise poses a challenge in many engineering applications due to its long wavelength, which makes conventional porous materials ineffective. In this paper, an acoustic metamaterial design consisting of multiple resonators periodically embedded within a porous material is proposed to effectively control multi-tonal low-frequency noise. Figure 1 presents the unit cell of the proposed metamaterial that consists of a porous material with embedded multiple Helmholtz resonators. In Fig. 1b, four different resonators are integrated within the porous material and Fig. 1c illustrates the porous layer with nine different embedded resonators. In Fig. 1d, sixteen different Helmholtz resonators are embedded within the porous layer and in Fig. 1a, the porous layer with one embedded resonator is shown for comparison. The cavities of the resonators have cylindrical shapes as well as

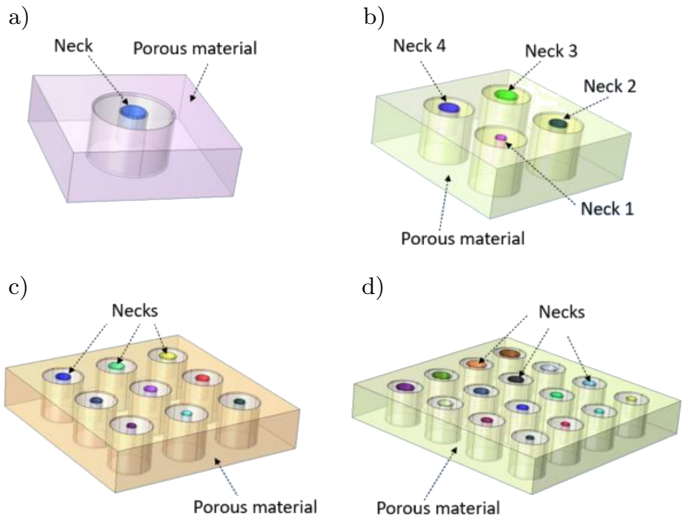


FIG. 1. Acoustic metamaterial based on porous layer with embedded multiple resonators: a) one periodic resonator, b) four periodic resonators, c) nine periodic resonators, d) sixteen periodic resonators.

the necks that are extended into the cavities. In Fig. 1, all the resonators have identical cavities with a diameter of 40 mm and in Fig. 1b, Fig. 1c, and Fig. 1d, the necks of the resonators have different geometric parameters illustrated by different colors while the cavities are separated from each other by an equal distance. The distance between the cavities axes of two adjacent resonators is 60 mm. In Fig. 1c, the nine cavities are identical and the geometric parameters of the nine necks are different, illustrated by different colors. Similarly, the sixteen cavities in Fig. 1d are identical with sixteen necks having different geometric parameters. The walls of the necks and the cavities in Fig. 1 are considered rigid and the thickness of the porous material is equal to the length of each resonator. The resonators are arranged in parallel within the porous material.

The sound attenuation performances of the metamaterial in Fig. 1 are studied numerically using COMSOL Multiphysics and the simulations are conducted with one periodic unit cell (PUC). Figure 2 shows the numerical models of the PUC for the transmission loss calculations. The PUC is made of an incident fluid, a transmission fluid and the porous layer with multiple embedded resonators. The incident and transmission fluids have identical length.

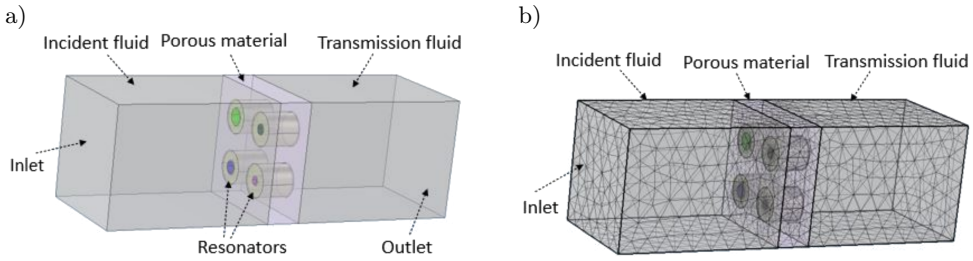


FIG. 2. PUC of the metamaterial: a) geometry with four HR, b) mesh with four HR.

A normal incidence plane wave with pressure amplitude of 1 Pa is imposed on the inlet plane in Fig. 2 and plane wave radiation condition is applied on the inlet and outlet planes while periodic boundary conditions are applied on all parallel planes in Fig. 2. The transmission loss is given by

$$\mathrm{TL} = 10 \log_{10} \left(\frac{W_i}{W_t} \right), \tag{1}$$

where W_t and W_i are the transmitted and incident sound power at the outlet and inlet planes, respectively.

Figure 3 presents the finite element models of the PUC for studying the diffuse field sound absorption performance of the metamaterial. The PUC in Fig. 3 consists of a perfectly matched layer (PML); a background

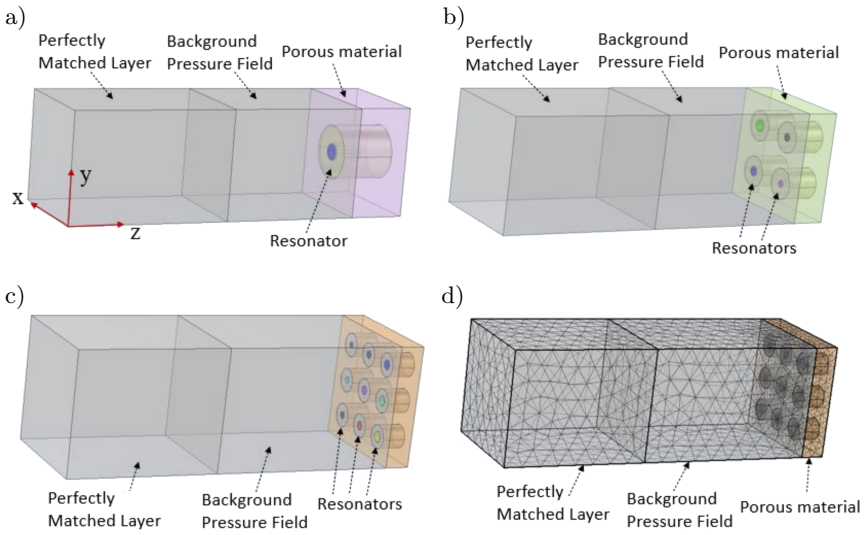


FIG. 3. PUC of the metamaterial for sound absorption estimation:
a) PUC with 1 HR, b) PUC with 4 HR, c) PUC with 9 HR, d) mesh with 9 HR.

acoustic pressure field and the porous material with embedded multiple resonators. Figure 3 shows, respectively, the PUC with one, four, nine resonators, and the mesh with nine resonators. The background pressure field provides an incident plane wave in the z-direction with an amplitude of 1 Pa, an incident angle θ, and an azimuthal angle ψ. The PML creates a virtual anechoic incident domain to eliminate the reflection of acoustic waves from the metamaterials.

The porous material as well as the air inside the neck of each resonator in Fig. 2 and Fig. 3 are modeled using the equivalent fluid model of Johnson–Champoux–Allard with the equivalent density $\rho_{eq}(\omega)$ and bulk modulus $K_{eq}(\omega)$ given by ALLARD and ATALLA (2009):

$$\rho_{eq}(\omega) = \alpha_\infty \rho_0 \left(1 + \frac{\sigma\phi}{j\omega\alpha_\infty\rho_0}\sqrt{1 + \frac{4j\rho_0\omega\eta\alpha_\infty^2}{\phi^2\sigma^2\Lambda^2}}\right), \tag{2}$$

$$K_{eq}(\omega) = \gamma P_0 \left[\gamma - \frac{\gamma - 1}{1 + \frac{8\eta}{j\omega\rho_0 \mathrm{Pr}\Lambda'^2}\sqrt{1 + \frac{j\omega\rho_0\mathrm{Pr}\Lambda'^2}{16\eta}}}\right]^{-1}, \tag{3}$$

where ϕ is the porosity, σ is the static airflow resistivity, α_∞ is the tortuosity, ρ_0 is the density, Λ is the viscous characteristic length, Λ' is the thermal characteristic length, η is the dynamic viscosity, Pr is the Prandtl number, γ is the specific heat ratio, and P_0 is the atmospheric static pressure. The tortuosity and the porosity of the air inside each neck are set to 1. The static airflow resistivity of the i-th neck is given by $\sigma_i = \frac{8\eta}{\phi_i R_i^2}$ with ϕ_i the porosity of the air inside the i-th neck and R_i the radius of the i-th neck whose viscous characteristic length is equal to R_i. The rest of the domains in Fig. 2 and Fig. 3 are characterized using the pressure acoustics module of COMSOL.

The oblique incident acoustic plane wave reaching the surface of the porous layer with embedded resonators is given by

$$P_i(\theta, \psi) = P_A e^{-j(k_x x + k_y y + k_z z)}, \tag{4}$$

where $P_A = 1$ Pa and j is the imaginary unit ($j^2 = -1$). The acoustic wave numbers k_x, k_y, and k_z in Eq. (4) are given by

$$\begin{cases} k_x = k_0 \sin\theta\cos\psi, \\ k_y = k_0 \sin\theta\sin\psi, \\ k_z = k_0 \cos\theta, \end{cases} \tag{5}$$

with $k_0 = \omega/c_0$, where ω is the angular frequency and c_0 is the speed of sound in air. Floquet periodic boundary conditions are imposed on all opposing parallel boundaries of the geometry in Fig. 3. The $\mathbf{k}$ wave vector for Floquet periodicity is given by $\mathbf{k} = [k_x\ k_y\ 0]$. The surface average of the total acoustic pressure P_t at the inlet surface of the metamaterial in Fig. 3 is determined numerically and the complex reflection coefficient is then obtained by

$$R(\theta,\psi) = \frac{P_t(\theta,\psi) - P_i(\theta,\psi)}{P_i(\theta,\psi)}. \tag{6}$$

The normalized surface acoustic impedance $Z_s(\theta,\psi)$ and the sound absorption coefficient $\alpha(\theta,\psi)$ of the metamaterial for each incidence angle θ are expressed by

$$Z_s(\theta,\psi) = \frac{1 + R(\theta,\psi)}{(1 - R(\theta,\psi))\cos(\theta,\psi)}, \qquad \alpha(\theta,\psi) = 1 - |R(\theta,\psi)|^2. \tag{7}$$

The diffuse field sound absorption coefficient for different incident waves with an incidence angle θ varying between 0 and $\theta_{\max}$, where $\theta_{\max}$ is the maximum incidence angle is then determined by (Laly *et al.*, 2025):

$$\alpha_D = \frac{\int_0^{\theta_{\max}} \alpha(\theta)\sin(2\theta)\,\mathrm{d}\theta}{\int_0^{\theta_{\max}} \sin(2\theta)\,\mathrm{d}\theta}. \tag{8}$$

A discretized form of this equation is used in the numerical calculations with $\theta_{\max}$ set to $\pi/2$ and the azimuthal angle ψ set to zero.

The thickness of the porous layer is set to 40 mm which is equal to the length of the cavity of each resonator. The static airflow resistivity of the porous layer is 26 000 $\mathrm{N\cdot s\cdot m^{-4}}$ with open porosity of 99 %, a tortuosity of 1.02 and the viscous and thermal characteristic lengths are respectively 150 µm and 300 µm. With one resonator within the porous material as shown in Fig. 3a, the radius of the neck is set to 4 mm with a length of 20 mm and the lateral dimensions of the PUC are set to 80 mm × 80 mm. For the metamaterial with four resonators embedded within the porous layer, the radii of the four necks are 4.5 mm, 5 mm, 5.5 mm, and 6 mm, respectively, with an identical length of 20 mm. In Fig. 3c where nine resonators are embedded within the porous layer, the radii of the nine resonators are, respectively, 4.5 mm, 5 mm, 5.5 mm, 6 mm, 6.5 mm, 7 mm, 7.5 mm, 8 mm, and 8.5 mm with the same length of 20 mm and the lateral dimensions of the PUC are 200 mm × 200 mm. In Fig. 3d, the length of the sixteen different necks of the resonators is equal to 20 mm and the radii are varied between 3 mm and 10.5 mm with a step of 0.5 mm.

3. Theoretical modeling

In this section, a theoretical approach is presented to model the porous material with embedded multiple resonators. Figure 4 shows the porous material with four embedded resonators having different necks illustrated by different colors. The periodic unit cell is divided into four regions denoted by layer 1 to layer 4 where the

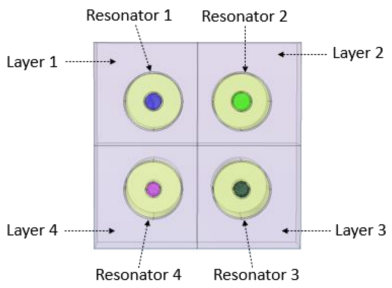


Fig. 4. Porous material with four embedded resonators.

lateral dimensions of each sub-porous layer i ($i = 1,2,3,4$) are $70\,\text{mm} \times 70\,\text{mm}$ and that of the unit cell are $140\,\text{mm} \times 140\,\text{mm}$. The layer i is made of the sub-porous layer i with the embedded resonator i.

The following assumptions are made:

– normal incidence plane wave propagation,
– there is no pressure diffusion between adjacent parallel elements,
– the wavelength is much longer than the PUC,
– each element namely the porous layer and each resonator can be modeled by a 2×2 transfer matrix.

The acoustic impedance of the Helmholtz resonator alone without the porous layer can be expressed as (Doutres *et al.*, 2015; Laly *et al.*, 2023):

$$Z_H^i = \frac{1}{s_e^i}\left(Z_{\text{neck}}^i - j s_v^i Z_0 \cot\left(kL_c^i\right)\right), \tag{9}$$

where Z_0 is the characteristic impedance of air, Z_{neck}^i is the impedance of the i-th neck, L_c^i is the i-th resonator cavity thickness, s_e^i and s_ν^i represent, respectively, the ratio of the i-th neck aperture surface over the cross section area of the i-th external elementary cell and an internal elementary cell. The acoustic impedance of the i-th neck is given by (Doutres *et al.* 2015; Laly *et al.*, 2024a; 2024b):

$$Z_{\text{neck}}^i = R_s\left(4 + \frac{2H_i}{R_i}\right) + j\omega\rho_0\left(\delta_i + \varepsilon_i + H_i\right), \tag{10}$$

where R_i and H_i are the radius and the length of the i-th neck, δ_i and ε_i are the correction lengths, and R_s is a surface resistance that is given by $R_s = 0.5\sqrt{2\eta\rho_0\omega}$. Since each resonator neck is circular, the approximation of the two corrections lengths for $s_e^i < 0.16$ is

$$\delta_i = \varepsilon_i = 0.48\sqrt{S_n^i}\left(1 - 1.14\sqrt{s_e^i}\right), \tag{11}$$

where S_n^i is the neck surface of the i-th resonator. The transfer matrix T_H^i of the i-th resonator can be written as

$$T_H^i = \begin{bmatrix} 1 & 0 \\ 1/Z_H^i & 1 \end{bmatrix}\begin{bmatrix} 1 & j\omega M_s^i \\ 0 & 1 \end{bmatrix} = \begin{bmatrix} T_{H11}^i & T_{H12}^i \\ T_{H21}^i & T_{H22}^i \end{bmatrix}, \tag{12}$$

where M_s^i is the mass per unit area of the i-th resonator ($M_s^i = \rho_0\left(\delta_i + \varepsilon_i + H_i\right)$). From Eq. (12), the admittance matrix Y_H^i of the i-th resonator can be obtained (Verdière *et al.*, 2013):

$$Y_H^i = \frac{1}{T_{H12}^i}\begin{bmatrix} T_{H22}^i & T_{H21}^i T_{H12}^i - T_{H22}^i T_{H11}^i \\ 1 & -T_{H11}^i \end{bmatrix}. \tag{13}$$

The transfer matrix T_p^i of each layer i of the porous material in Fig. 4 is determined using the equivalent density $\rho_{eq}(\omega)$ and the bulk modulus $K_{eq}(\omega)$ given by Eq. (2) and Eq. (3). It is expressed by

$$T_P^i = \begin{bmatrix} \cos\left(k_{eq}^i L_i\right) & j Z_{eq}^i \sin\left(k_{eq}^i L_i\right) \\ j\dfrac{\sin\left(k_{eq}^i L_i\right)}{Z_{eq}^i} & \cos\left(k_{eq}^i L_i\right) \end{bmatrix} = \begin{bmatrix} T_{P11}^i & T_{P12}^i \\ T_{P21}^i & T_{P22}^i \end{bmatrix}, \tag{14}$$

where L_i is the thickness of the i-th layer, Z_{eq}^i and k_{eq}^i are the characteristic impedance and the wave number of the equivalent fluid of the i-th layer given by

$$Z_{eq}^i = \sqrt{\rho_{eq} K_{eq}}/\phi, \qquad k_{eq}^i = \omega\sqrt{\rho_{eq}/K_{eq}}. \tag{15}$$

From Eq. (15), the admittance matrix Y_p^i of each layer of the porous material in Fig. 4 is obtained. It is given by

$$Y_P^i = \frac{1}{T_{P12}^i}\begin{bmatrix} T_{P22}^i & T_{P21}^i T_{P12}^i - T_{P22}^i T_{P11}^i \\ 1 & -T_{P11}^i \end{bmatrix}. \tag{16}$$

Each i-th layer of porous material with the embedded i-th resonator in Fig. 4 are assembled in parallel, so their equivalent transfer matrix M^i is determined using the parallel transfer matrix method (Verdière *et al.*, 2013):

$$M^i = \frac{-1}{\sum r_n^i Y_{n21}^i}\begin{bmatrix} \sum r_n^i Y_{n22}^i & -1 \\ \sum r_n^i Y_{n22}^i \sum r_n^i Y_{n11}^i - \sum r_n^i Y_{n12}^i \sum r_n^i Y_{n21}^i & -\sum r_n^i Y_{n11}^i \end{bmatrix}, \tag{17}$$

where Y_n^i represents the admittance matrix components of Eq. (13) and Eq. (16) with $n = H$ for the resonator and $n = P$ for the porous substrate and r_n^i is the surface ratio of each element given by

$$r_H^i = S_i / S_P^i, \qquad r_P^i = 1 - r_H^i, \tag{18}$$

where S_P^i is the surface of the i-th unit cell layer and S_i is the surface of the i-th resonator. The transfer matrices of layer 1, layer 2, layer 3, and layer 4 in Fig. 4 are then, respectively, denoted by M^1, M^2, M^3 and M^4. Thus, the admittance matrix of each i-th layer in Fig. 4 is obtained from Eq. (17) and is expressed by

$$Y^i = \frac{1}{M_{12}^i}\begin{bmatrix} M_{22}^i & M_{21}^i M_{12}^i - M_{22}^i M_{11}^i \\ 1 & -M_{11}^i \end{bmatrix}. \tag{19}$$

In Fig. 4, layer 1 and layer 2 are assembled in parallel, thus the equivalent transfer matrix TM^a of layer 1 and layer 2 is determined by

$$TM^a = \frac{-1}{\sum r_m Y_{21}^m}\begin{bmatrix} \sum r_m Y_{22}^m & -1 \\ \sum r_m Y_{22}^m \sum r_m Y_{11}^m - \sum r_m Y_{12}^m \sum r_m Y_{21}^m & -\sum r_m Y_{11}^m \end{bmatrix}. \tag{20}$$

In Eq. (20), $m = 1, 2$, Y^m is obtained from Eq. (19), $r_1 = S_1^L / S_{12}^L$, $r_2 = 1 - r_1$ with S_1^L the surface of layer 1 and S_{12}^L the surface of both layer 1 and layer 2.

Similarly, layer 3 and layer 4 in Fig. 4 are assembled in parallel, so their equivalent transfer matrix TM^b is given by

$$TM^b = \frac{-1}{\sum r_u Y_{21}^u}\begin{bmatrix} \sum r_u Y_{22}^u & -1 \\ \sum r_u Y_{22}^u \sum r_u Y_{11}^u - \sum r_u Y_{12}^u \sum r_u Y_{21}^u & -\sum r_u Y_{11}^u \end{bmatrix}, \tag{21}$$

where $u = 3, 4$, Y^u is given by Eq. (19), $r_3 = S_3^L / S_{34}^L$, $r_4 = 1 - r_3$ with S_3^L the surface of layer 3 and S_{34}^L the surface of both layer 3 and layer 4. If the parallel assembly of layer 1 and layer 2 is denoted by material A and the parallel assembly of layer 3 and layer 4 by material B, then materials A and B are arranged in parallel and their admittance matrices can be expressed as

$$YM^q = \frac{1}{TM_{12}^q}\begin{bmatrix} TM_{22}^q & TM_{21}^q TM_{12}^q - TM_{22}^q TM_{11}^q \\ 1 & -TM_{11}^q \end{bmatrix}. \tag{22}$$

In Eq. (22), $q = a, b$ and TM^q is obtained from Eq. (20) and Eq. (21). The transfer matrix of the porous material with four embedded Helmholtz resonators, in Fig. 4, is finally determined by

$$TG = \frac{-1}{\sum r_q YM_{21}^q}\begin{bmatrix} \sum r_q YM_{22}^q & -1 \\ \sum r_q YM_{22}^q \sum r_q YM_{11}^q - \sum r_q YM_{12}^q \sum r_q YM_{21}^q & -\sum r_q YM_{11}^q \end{bmatrix}. \tag{23}$$

The transfer matrix in Eq. (23) can be expressed as $TG = \begin{bmatrix} TG_{11} & TG_{12} \\ TG_{21} & TG_{22} \end{bmatrix}$. The theoretical sound absorption coefficient α_{theo} of the metamaterial in Fig. 4 can be calculated using the components of the matrix TG:

$$\alpha_{\text{theo}} = 1 - \left| \frac{TG_{11} - Z_0\, TG_{21}}{TG_{11} + Z_0\, TG_{21}} \right|^2 . \tag{24}$$

The theoretical transmission loss TL_{theo} of the metamaterial consisting of the porous layer with four embedded resonators is obtained from Eq. (23) and is given by

$$\text{TL}_{\text{theo}} = -20 \log_{10} \left| \frac{2}{TG_{11} + TG_{12}/Z_0 + Z_0\, TG_{21} + TG_{22}} \right|. \tag{25}$$

4. Comparison of the finite element method and the theory

In this section, the sound absorption coefficient and the TL predicted theoretically using Eq. (24) and Eq. (25) are compared with the results of the finite element method. Figure 5 presents the comparison of the sound absorption coefficient of the metamaterial of Fig. 1a made of porous material with one embedded periodic resonator and the comparison of the corresponding TL is shown in Fig. 6. The absorption coefficient of the material with one embedded resonator presents a peak of 0.9 at 364 Hz while without the resonator the absorption coefficient value is 0.34 at 364 Hz. The theoretical calculation agrees well with the FEM. In Fig. 6, the FEM result of the TL with the resonator shows a peak of 18 dB at 364 Hz and the theoretical TL peak at this frequency is 17 dB. Without the resonator, the TL of the porous material alone is lower than 8 dB over the entire frequency range.

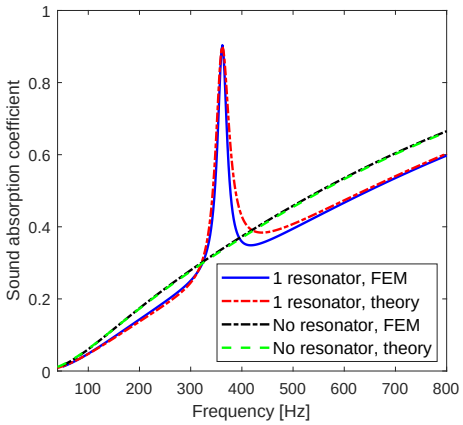


Fig. 5. Comparison of the sound absorption coefficient of the metamaterial with one embedded resonator.

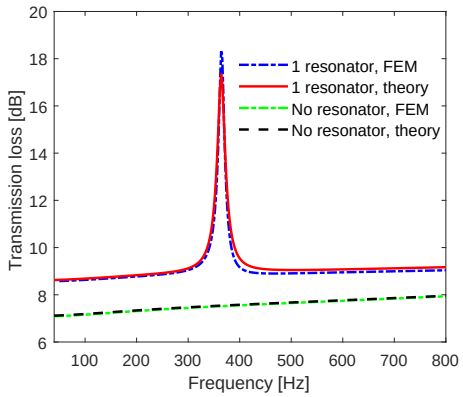


Fig. 6. Comparison of the transmission loss of the metamaterial with one embedded resonator.

Figure 7 presents the comparison of the theoretical absorption coefficient and the FEM result for the metamaterial of Fig. 1b consisting of the porous layer with four embedded different resonators and the comparison of the corresponding TL is shown in Fig. 8. The absorption coefficient as well as the TL exhibit four resonance peaks at 408 Hz, 448 Hz, 490 Hz, and 530 Hz. The FEM peak values of the sound absorption are 0.98, 0.99, 0.98, and 0.92, respectively, while the theoretical values are 0.94, 0.99, 0.99, and 0.97. The peaks of the TL predicted by the FEM are 13 dB, 14 dB, 15.2 dB, and 16 dB, respectively, and for the theory, the peaks of the TL are 12.7 dB, 13.5 dB, 14 dB, and 15 dB. The results of the theory and the FEM in Fig. 7 and Fig. 8 are in good agreement. With four parallel resonators embedded within the porous layer, the sound absorption and the TL present four different resonant peaks while only one resonant peak is observed in Fig. 5 and Fig. 6 for one resonator incorporated within the porous material.

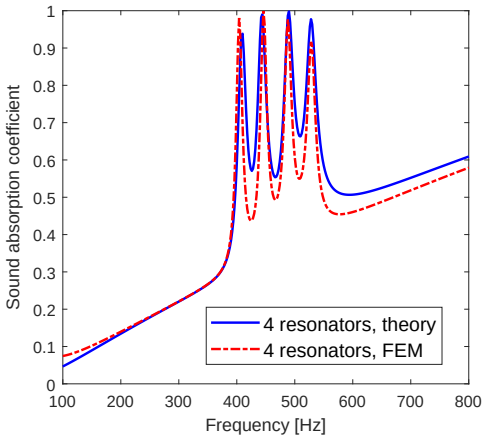


FIG. 7. Comparison of the sound absorption coefficient of the metamaterial with four embedded resonators.

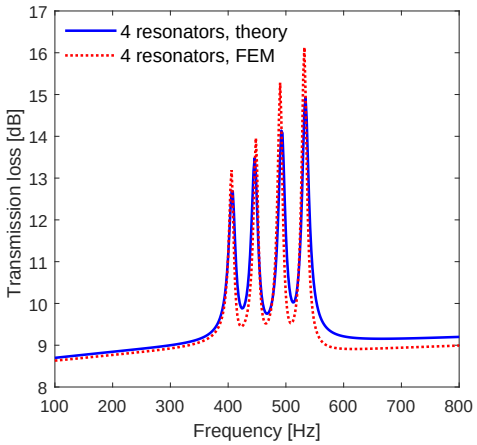


FIG. 8. Comparison of the transmission loss of the metamaterial with four embedded resonators.

For a plane wave impinging on the metamaterial surface with an incidence angle θ, the theoretical sound absorption coefficient and the transmission loss can be determined by (VERDIÈRE *et al.*, 2013):

$$\alpha_\theta = 1 - \left| \frac{T_{11}\cos\theta - Z_0 T_{21}}{T_{11}\cos\theta + Z_0 T_{21}} \right|^2, \tag{26}$$

$$\mathrm{TL}_\theta = 20\log_{10}\left(\frac{1}{2}\left|\left(T_{11} + \frac{T_{12}\cos\theta}{Z_0} + \frac{Z_0 T_{21}}{\cos\theta} + T_{22}\right)\right|\right). \tag{27}$$

In Eq. (26) and Eq. (27), T_{11}, T_{12}, T_{21}, and T_{22} are the components of the global matrix of the metamaterial made of the porous layer with embedded resonators that can be obtained using Eq. (17) and Eq. (23). Figure 9 presents the comparison of the sound absorption coefficient of the porous layer with one and four

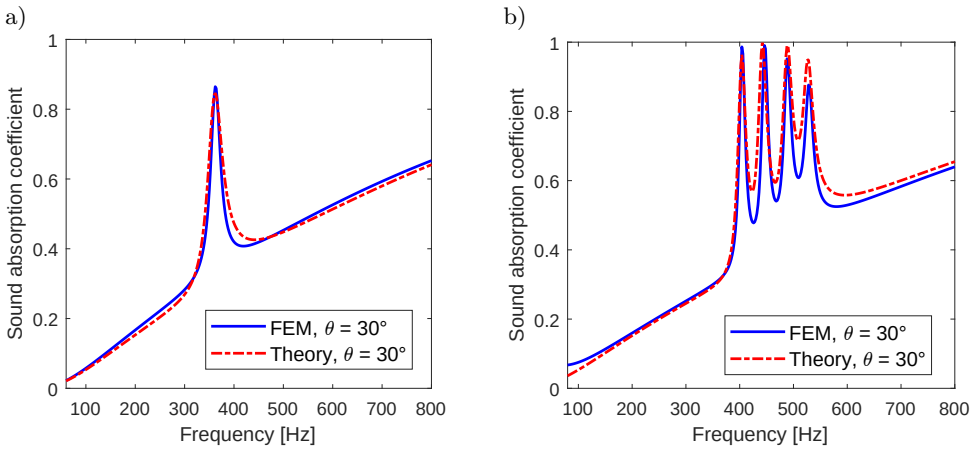


FIG. 9. Sound absorption coefficient for oblique incidence: a) one embedded resonator, b) four embedded resonators.

embedded resonators for an incidence angle of 30°. It can be observed that the oblique incidence sound absorption predicted theoretically agrees with the FEM.

Figure 10a and Fig. 10b show the porous material with four embedded resonators and the distance L separating the axes of two adjacent resonators is varied to analyze the interaction effect between the resonators. Figure 10c, Fig. 10d, and Fig. 10e illustrate the porous material with one, four, and nine perforations in place of the resonators. The diameter of each perforation is identical to the diameter of the cavity of each resonator, which is 40 mm. The absorption coefficient of the porous material with embedded resonators and with perforations is studied in the following section. In Fig. 10a and Fig. 10b, the lateral dimensions are 200 mm × 200 mm and the distance between the axes of two adjacent resonators is set to 45 mm in Fig. 10a, while it is 110 mm in Fig. 10b. The normal incidence sound absorption coefficient of these two configurations is illustrated in Fig. 11, where configuration A represents the case of L equal to 45 mm. With configuration A, the values of the first and fourth absorption peaks are 0.86 and 0.97, while they are 0.83 and 0.98, respectively, for configuration B. A slight difference is also observed for frequencies above 550 Hz that should be caused by the interaction effect between the resonators, which is not considered in the analytical model. The minor deviation observed between the theoretical model and the FEM results in Fig. 7 and Fig. 8 may also result from coupling effects between the resonators.

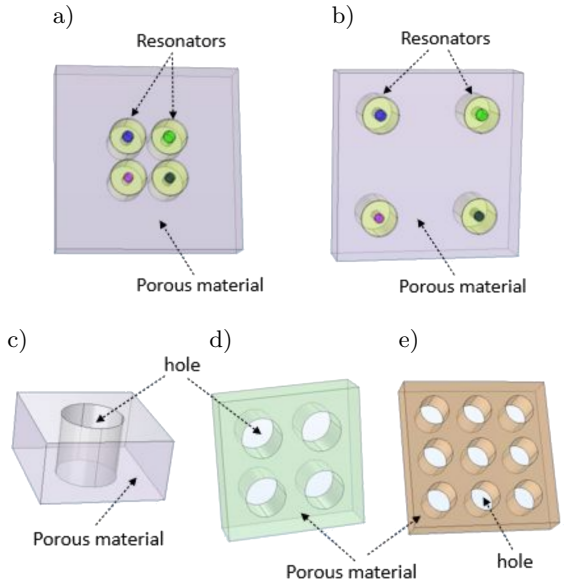


FIG. 10. Geometrical models of: a) porous layer with four resonators, L = 45 mm, b) porous layer with four resonators, L = 110 mm, c) porous layer with one perforation, d) porous layer with four perforations, e) porous layer with nine perforations.

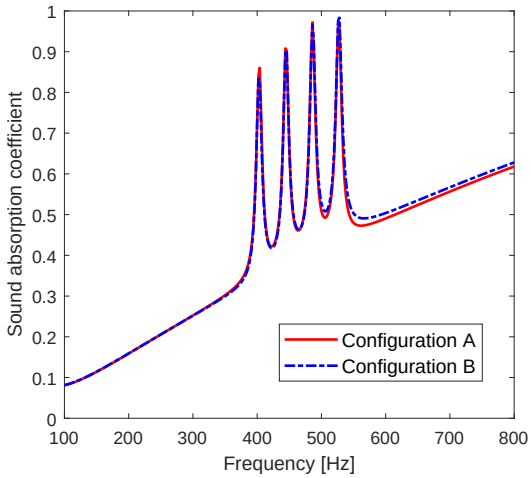


FIG. 11. Sound absorption coefficient.

5. Analysis of the sound attenuation performance

In this section, the sound attenuation performance of the proposed metamaterial is studied numerically. The diffuse field sound absorption coefficient is obtained using Eq. (8) where $\theta_{\max}$ is set to $\pi/2$.

Figure 12 shows the sound absorption coefficient of the porous layer with one embedded periodic Helmholtz resonator (Fig. 1a) at different oblique incidence angles θ. The sound absorption coefficients of the porous layer without resonators and with one and four perforations in the place of resonators as illustrated in Fig. 10c and Fig. 10d are also presented. The normal incidence sound absorption coefficient in Fig. 12 presents a resonant peak of 0.9 at 362 Hz. For $\theta = 60°$, the absorption coefficient shows a peak of 0.77 at 372 Hz while the diffuse field sound absorption coefficient presents a peak of 0.76 at 364 Hz. The normal incidence sound absorption coefficient of the porous material alone is lower than 0.5 for frequencies below 500 Hz. With one or four perforations within the porous layer, the sound absorption is lower than that of porous layer alone.

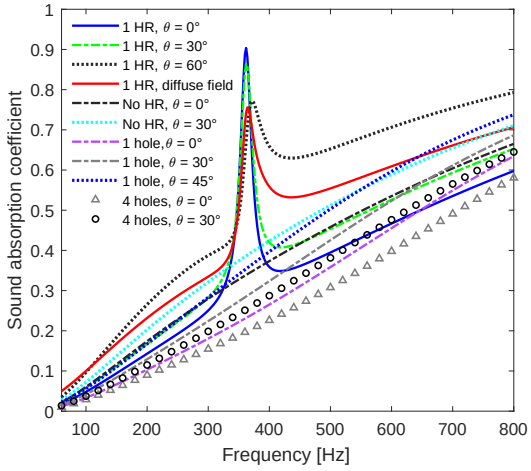


FIG. 12. Sound absorption coefficient of the metamaterial.

Figure 13 shows the oblique incidence and the diffuse field sound absorption coefficient of the porous material with four different incorporated resonators as illustrated in Fig. 1b. As θ increases up to 40°, the sound absorption coefficient with 4 HR shows four identical resonant frequencies of 408 Hz, 448 Hz, 490 Hz, and 530 Hz. The sound absorption peaks at these four resonant frequencies are 0.98, 0.99, 0.976, and 0.92, respectively, for $\theta = 0°$ while for $\theta = 40°$, they are 0.985, 0.99, 0.94, and 0.84. The diffuse field sound absorption with 4 HRs presents four resonant peaks of 0.95, 0.94, 0.87, and 0.76, respectively, at the resonant frequencies, while without HR, the values of the absorption coefficient at the resonant frequencies are 0.5, 0.53, 0.57, and 0.6, respectively. Above 70°, the

absorption coefficient is lower as the incidence angle increases. Indeed, for an incidence angle of 88°, the absorption coefficient without HR is lower than 0.2 and presents four peaks of 0.28, 0.3, 0.32, and 0.4 with 4 HRs.

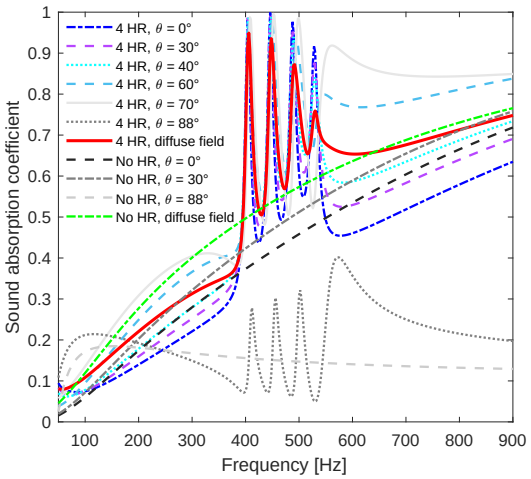


FIG. 13. Diffuse field sound absorption of the metamaterial with four embedded resonators.

The sound absorption coefficient at various incidence angles as well as the diffuse field absorption coefficient of the metamaterial in Fig. 1c made of porous material with nine embedded resonators are shown in Fig. 14 and compared to the sound absorption without the resonators. The corresponding normal incidence TL is presented in Fig. 15 as well as the TL of the porous layer alone and that of the porous layer with nine perforations. When θ increases up to 50°, the absorption coefficient in Fig. 14 with 9 HRs presents nine resonant frequencies around 408 Hz, 448 Hz, 490 Hz, 530 Hz, 572 Hz, 612 Hz, 654 Hz, 694 Hz, and 734 Hz. The absorption peak values for normal incidence in Fig. 14 are 0.82, 0.9, 0.94, 0.98, 0.98, 0.99, 0.984, 0.98, and 0.95 while the diffuse field absorption peak values are 0.87, 0.9, 0.93, 0.94, 0.95, 0.96, 0.91, 0.9, and 0.87, respectively. Without the embedded resonators, the diffuse field absorption coefficient increases from 0.47 at 370 Hz to 0.73 at 800 Hz. The absorption coefficient is significantly improved at the nine resonant frequencies of the nine resonators. The TL of the metamaterial with 9 HR in Fig. 15 exhibits nine resonance peaks of 12.9 dB, 14.4 dB, 14 dB, 15.7 dB, 18 dB, 15.7 dB, 16 dB 16.5 dB, and 13 dB at the resonance frequencies and outside these frequencies the TL is about 9 dB while without the resonators, the TL is between 7 and 8 dB. The TL of the porous layer with nine perforations is lower than 5 dB over the entire frequency range. The diffuse field sound absorption and the TL in Fig. 14 and Fig. 15 are significantly enhanced at the resonance frequencies of the resonators. Compared to Fig. 13, it can be observed that the frequency band of the absorption coefficient increases as the number of resonators within the unit cell increases.

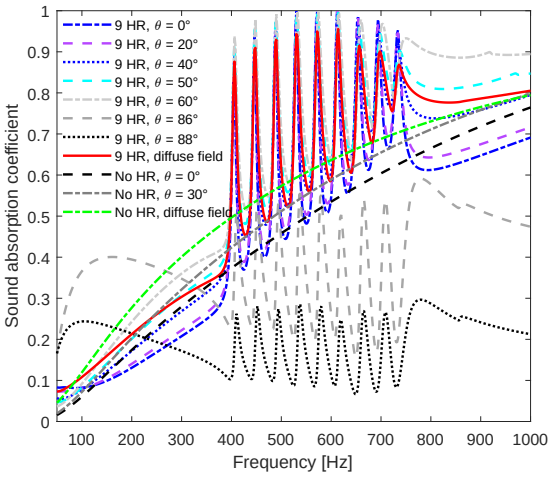


FIG. 14. Diffuse field sound absorption of the metamaterial with nine embedded resonators.

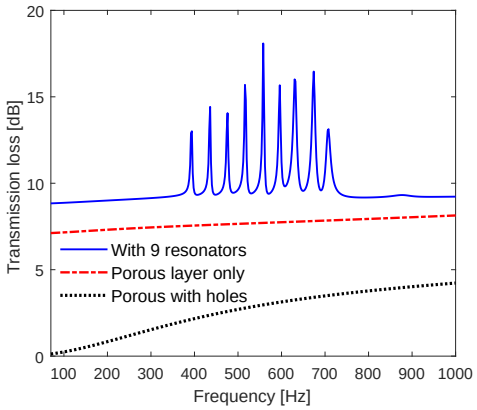


FIG. 15. Transmission loss of the metamaterial with nine embedded resonators.

Figure 16 shows the absorption coefficient at different incidence angles and the diffuse field sound absorption of the porous material with sixteen different embedded resonators as illustrated in Fig. 1d. With sixteen embedded resonators, the absorption coefficient for each incidence angle shows sixteen resonance peaks in Fig. 16 with the peak values that are between 0.54 and 0.95 for the diffuse field sound absorption. The frequency band of the sound absorption in Fig. 16 is larger than the one in Fig. 14 for the porous layer with nine embedded resonators. The absorption coefficient decreases mainly when the incidence angle is higher than 75°.

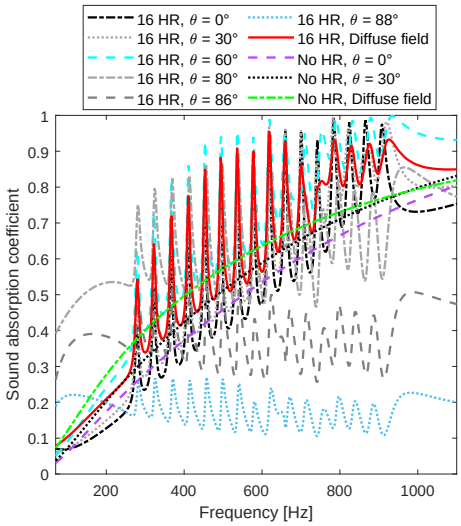


FIG. 16. Diffuse field sound absorption of the metamaterial with sixteen embedded resonators.

The sound attenuation mechanism of the metamaterial is investigated in the following. One considers the material design of Fig. 1b where the PUC is made of four parallel resonators that are incorporated into the porous layer. The sound absorption coefficient in Fig. 13 showed four resonant peaks at 408 Hz, 448 Hz, 490 Hz, and 530 Hz, and when the incidence angle is greater than 70°, the absorption coefficient decreases. Figure 17 illustrates the total root mean square (RMS) acoustic pressure through the metamaterial at 300 Hz, 408 Hz, 448 Hz, 490 Hz, 530 Hz, and 700 Hz for incidence angles of 0° and 75°. The total acoustic velocity at the four resonant frequencies are shown in Fig. 18, while Fig. 19 presents the acoustic power dissipation density.

For a normal incidence, it is observed in Fig. 17a that the RMS acoustic pressure at each resonance frequency reaches its maximum value in the cavity of the corresponding resonator and is 30 Pa. Outside these resonance frequencies the acoustic pressure is very low in the cavities. The acoustic velocity in Fig. 18 reaches a maximum value 0.4 m/s in the neck of each resonator at the corresponding resonance frequency and the acoustic power dissipation density is significant in the neck at the resonance frequency. As the frequency increases above the highest resonance frequency associated with HRs, the power dissipation density in the porous layer reaches its

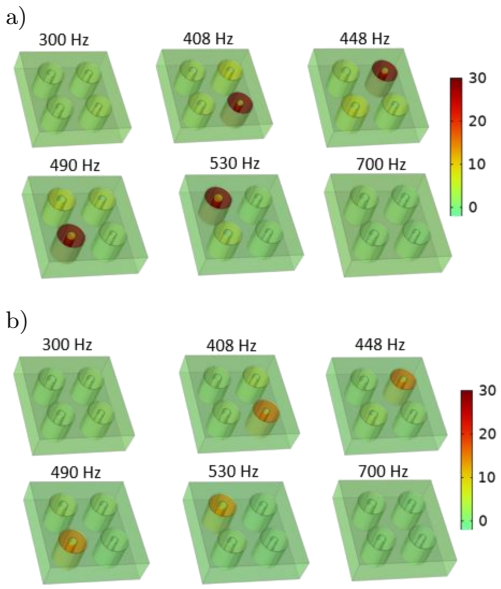


FIG. 17. Total RMS acoustic pressure [Pa]: a) $\theta = 0°$, b) $\theta = 75°$.

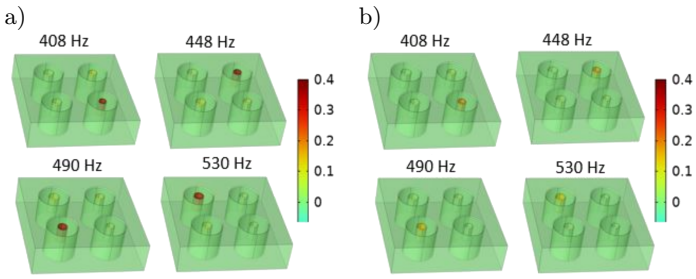


FIG. 18. Total acoustic velocity [m/s]: a) $\theta = 0°$, b) $\theta = 75°$.

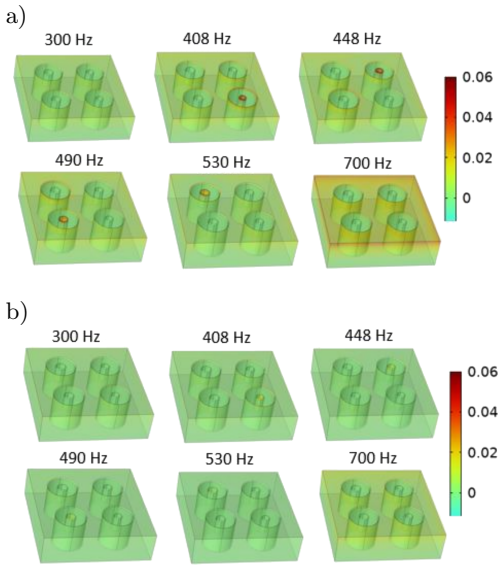


FIG. 19. Acoustic power dissipation density [W/m^3]: a) $\theta = 0°$, b) $\theta = 75°$.

highest value, and sound absorption is mainly due to the porous material matrix. The four parallel resonators act independently resulting in four absorption peaks. For an incidence angle of 75°, the acoustic pressure in the cavities at the resonance frequencies decreases, the acoustic velocity in the necks (Fig. 18b) becomes low and the power dissipation density is negligible in Fig. 19b and consequently the absorption coefficient becomes low as observed in Fig. 13.

6. Conclusion

A design of acoustic metamaterial made of porous material with multiple embedded Helmholtz resonators was proposed and studied for multi-tonal and broadband noise reduction. A theoretical approach based on the transfer matrix method was presented and the theoretical results of the sound absorption and the transmission loss showed good agreement with the FEM. Compared to the porous layer with one embedded Helmholtz resonator that presents one resonant peak, the metamaterial consisting of the porous material with four, nine, and sixteen embedded Helmholtz resonators exhibits respectively four, nine, and sixteen sound absorption and TL resonant peaks. The impacts of the incidence angles were demonstrated and the diffuse field sound absorption was significantly improved at the resonant frequencies of the resonators. The TL and the sound absorption frequency band increase as the number of resonators within the porous layer increases. The proposed metamaterial can help in multiple engineering applications for multi-tonal and broadband noise attenuation.

Fundings

This research did not receive any specific grant from funding agencies in the public, commercial, or not-for-profit sectors.

Conflict of interest

The authors declare that there are no known competing financial interests or personal relationships that could have influenced the work described in this paper.

Authors' contributions

Zacharie Laly contributed to conceptualization, investigation, methodology, data analysis and interpretation, validation, and writing. Raymond Panneton contributed to supervision, project administration, resources, data analysis and interpretation, review and editing. Noureddine Atalla contributed to supervision, project administration, resources, data analysis and interpretation, review and editing. Sebastian Ghinet contributed to investigation, data analysis and interpretation, review and editing. All authors reviewed and approved the final manuscript.

References

1. Abbad A., Atalla N., Ouisse M., Doutres O. (2019), Numerical and experimental investigations on the acoustic performances of membraned Helmholtz resonators embedded in a porous matrix, *Journal of Sound and Vibration*, **459**: 114873, https://doi.org/10.1016/J.JSV.2019.114873.
2. Allard J.F., Atalla N. (2009), *Propagation of Sound in Porous Media: Modelling Sound Absorbing Materials*, John Wiley & Sons, https://doi.org/10.1002/9780470747339.
3. Boutin C., Becot F.X. (2015), Theory and experiments on poro-acoustics with inner resonators, *Wave Motion*, **54**: 76–99, https://doi.org/10.1016/J.WAVEMOTI.2014.11.013.
4. Doutres O., Atalla, N., Osman H. (2015), Transfer matrix modeling and experimental validation of cellular porous material with resonant inclusions, *The Journal of the Acoustical Society of America*, **137**(6): 3502–3513, https://doi.org/10.1121/1.4921027.
5. Ghinet S., Bouche P., Padois T., Pires L. (2020), Experimental validation of acoustic metamaterials noise attenuation performance for aircraft cabin applications, [in:] *Proceedings of 2020 International Congress on Noise Control Engineering*.
6. Kone T.C., Ghinet S., Panneton R., Grewa A. (2021), Optimization of metamaterials with complex neck shapes for aircraft cabin noise improvement, [in:] *INTER-NOISE and NOISE-CON Congress and Conference Proceedings*, https://doi.org/10.3397/IN-2021-2567.

7. Kone T.C., Ghinet S., Panneton R., Laly Z., Mechefske C., Grewal A. (2022), Control and broadening of multiple noise frequencies using an assembly of sub-metamaterials connected by membranes for aircraft noise mitigation, [in:] *INTER-NOISE and NOISE-CON Congress and Conference Proceedings*, https://doi.org/10.3397/IN_2022_0663.

8. Lagarrigue C., Groby J.P., Tournat V., Dazel O., Umnova O. (2013), Absorption of sound by porous layers with embedded periodic arrays of resonant inclusions, *The Journal of the Acoustical Society of America*, **134**(6): 4670–4680, https://doi.org/10.1121/1.4824843.

9. Laly Z., Mechefske C., Ghinet S., Kone C.T. (2024a), Finite element modeling of acoustic metamaterial based on periodic Helmholtz resonator with a membrane in the cavity, *Noise Control Engineering Journal*, **72**(6): 514–542, https://doi.org/10.3397/1/377239.

10. Laly Z., Mechefske C., Ghinet S., Kone C.T., Atalla N. (2023), Design and analysis of periodic acoustic metamaterial sound insulator using finite element method, *Noise Control Engineering Journal*, **71**(5): 344–364, https://doi.org/10.3397/1/377128.

11. Laly Z., Mechefske C., Ghinet S., Kone C.T., Panneton R., Atalla N. (2025), Diffuse field sound absorption performance of porous material with embedded periodic Helmholtz resonators, [in:] *INTER-NOISE and NOISE-CON Congress and Conference Proceedings*, https://doi.org/10.3397/in_2025_1074286.

12. Laly Z., Mechefske C., Ghinet S., Kone C.T., Atalla N., Ashrqafi B. (2024b), The effects of Helmholtz resonator wall elasticity on the sound attenuation performance, *Noise Control Engineering Journal*, **72**(6): 543–563, https://doi.org/10.3397/1/377240.

13. Laly Z., Panneton R., Atalla N. (2022), Characterization and development of periodic acoustic metamaterials using a transfer matrix approach, *Applied Acoustics*, **185**: 108381, https://doi.org/10.1016/J.APACOUST.2021.108381.

14. Magliacano D., Catapane G., Petrone G., Verdière K., Robin O. (2024), Sound transmission properties of a porous meta-material with periodically embedded Helmholtz resonators, *Mechanics of Advanced Materials and Structures*, **31**(25): 6748–6756, https://doi.org/10.1080/15376494.2023.2237699.

15. Verdière K., Panneton R., Elkoun S., Dupont T., Leclaire P. (2013), Transfer matrix method applied to the parallel assembly of sound absorbing materials, *The Journal of the Acoustical Society of America*, **134**(6): 4648–4658, https://doi.org/10.1121/1.4824839.

16. Zhang W., Xin F. (2024), Broadband low-frequency sound absorption via Helmholtz resonators with porous material lining, *Journal of Sound and Vibration*, **578**: 118330, https://doi.org/10.1016/J.JSV.2024.118330.

17. Zhu X.F., Lau S.-K., Lu Z., Jeon W. (2019), Broadband low-frequency sound absorption by periodic metamaterial resonators embedded in a porous layer, *Journal of Sound and Vibration*, **461**: 114922, https://doi.org/10.1016/J.JSV.2019.114922.